JOURNAL OF AIRCRAFT
Vol. 45, No. 4, July–August 2008

# Transonic Nonlinear Aeroelastic Analysis of Aircraft Tail Wings Using Multiblock Approach

Jong-Yun Kim,* Kyung-Seok Kim,* Seung-Jun Lee,* and In Lee†
*Korea Advanced Institute of Science and Technology, Daejeon 305-701, Republic of Korea*
and
Seung-Kil Paek‡
*Korea Aerospace Research Institute, Daejeon 305-333, Republic of Korea*

DOI: 10.2514/1.34824

**An aeroelastic analysis of a model that uses a combination of horizontal and vertical tails is performed in a transonic flow regime. A transonic small disturbance equation is used for the aerodynamic analysis. The combined model is divided into horizontal tail and vertical tail blocks because the transonic small disturbance equation can only be applied to models with lifting surfaces on identical or parallel planes. Nonmatching grid points are positioned on each interface between the horizontal and vertical tail blocks. To form a transonic small disturbance equation continuously at the interfaces, each block requires imaginary planes with potential interfaces with the adjacent block and the grid points on the block interface. A bivariate interpolation method was used to construct the imaginary planes. The aerodynamic analysis results of the combined model are compared with the results obtained from Euler equations. The results show that the transonic small disturbance equation can be used in an aerodynamic analysis of a combined model with horizontal and vertical lifting surfaces. Finally, the aeroelastic characteristics of the horizontal tail are investigated using comparisons of the time responses between the combined model and the horizontal tail model.**

## Nomenclature

| | | |
|---|---|---|
| $C_p$ | = | pressure coefficient |
| $[C]$ | = | damping matrix |
| $[C_g]$ | = | generalized damping matrix |
| $c_r$ | = | root chord length |
| $h$ | = | vibration mode shape |
| $[K]$ | = | stiffness matrix |
| $[K_g]$ | = | generalized stiffness matrix |
| $M$ | = | freestream Mach number |
| $[M]$ | = | mass matrix |
| $[M_g]$ | = | generalized mass matrix |
| $\{\mathbf{Q}_g\}$ | = | generalized aerodynamic forces vector |
| $\{\mathbf{q}\}$ | = | generalized modal displacement vector |
| $t$ | = | time, nondimensionalized by $U/c_r$ |
| $U$ | = | freestream velocity |
| $x, y, z$ | = | nondimensional physical coordinates in the streamwise, spanwise, and vertical directions, respectively |
| $\gamma$ | = | specific heat ratio |
| $\rho$ | = | freestream density |
| $\phi$ | = | disturbance velocity potential |

## I. Introduction

AIRCRAFT experience aeroelastic problems in flight due to the interaction between structures and aerodynamic forces. Aeroelasticity is concerned with the interaction phenomena between the elastic motions of structures and the resulting aerodynamic forces [1]. Such a mutual interaction can exist for flying aircraft. There are many categories of aeroelastic phenomena according to physical features, including flutter, divergence, gust response, buffeting, limit cycle oscillations, and others. All of these should be considered in aircraft design because the structural flexibility resulting from light materials in modern aircraft is more susceptible to aeroelastic phenomena. Among the aforementioned categories, flutter is the most dangerous dynamic problem, as the occurrence of flutter can result in complete structural failure within seconds. Modern aircraft are usually designed to cover a wide flight envelope, and they experience intense flow characteristic changes when they pass through transonic flow regions. Flutter instability is usually aggravated in transonic and low supersonic regions and is closely related to the unstable movement of shock waves. Hence, it is important to consider the effects of normal shock waves for accurate prediction of flutter characteristics.

To achieve accurate aeroelastic analyses in transonic flow regions, the computational fluid dynamics (CFD) technique must be used due to aerodynamic nonlinearity issues such as moving shock. In particular, to capture the full nonlinearity of a flowfield including, for example, the viscous effect, Navier–Stokes equations using a turbulent model should be applied to the aeroelastic analysis. However, these equations, like Euler equations, are difficult to apply to three-dimensional configurations and incur a high computational cost, as arbitrary elastic motion with control surface rotation presents a very challenging problem in treating the mesh and guaranteeing numerical stability [2]. Moreover, when an aeroelastic analysis with the local motion of the control surface is conducted in a transonic flow region, a long response time is usually required to determine the aeroelastic stability clearly. Therefore, an aeroelastic examination using an efficient unsteady aerodynamic analysis, such as the transonic small disturbance (TSD) equation, which is widely recognized as one of the most efficient theories among the conventional CFD-based approaches, can have strong computational advantages in many different types of parametric studies [3]. Additionally, the TSD equation simplifies grid generation, as only the slope values of lifting surfaces are needed on each grid point. In particular, it does not require additional grid remeshing processes as it uses the changes in the airfoil slopes at each wall grid point to simulate arbitrary wing surface motions [4].

Received 27 September 2007; revision received 7 January 2008; accepted for publication 12 January 2008. 

*Graduate Research Assistant, Department of Aerospace Engineering, KAIST, 335 Gwahangno, Yuseong-gu.

†Professor, Ph.D., Department of Aerospace Engineering, 335 Gwahangno, Yuseong-gu; Corresponding Author. AIAA Associate Fellow.

‡Senior Researcher, Ph.D., Rotor Department, Korean Helicopter Program Development Division, Aeronautics Program Office, 45 Eoeun-dong, Yuseong-gu.

For the past few decades, research on aeroelastic analysis has been conducted using the TSD equation for various aircraft models [5–9]. Particularly, Batina formulated a time-accurate approximate factorization (AF) algorithm as a solution of the three-dimensional unsteady TSD equation [10]. Thereafter, Batina et al. laid the cornerstone of practical aeroelastic analysis for three-dimensional aircraft models as the transonic unsteady aerodynamics, and the aeroelastic code was developed for application in realistic aircraft configurations [11]. However, most unsteady aerodynamic and aeroelastic analyses using the TSD equation are applied only in models with lifting surfaces in identical or parallel planes, as the derived TSD equation restricts the swept finite difference mesh in the vertical direction of the lifting surfaces [12]. Under these conditions, the TSD equation is one factor that gives computational efficiency. Thus, it is difficult to find aeroelastic research that considers combined models with horizontal and vertical lifting surfaces, and there have been few trials in which aerodynamic analysis using the TSD equation was performed for models that consider both horizontal and vertical lifting surfaces. Gibbons extended the TSD equation to the vertical direction and unsteady aerodynamic analysis was accomplished for rectangular and swept T-tails [13]. To perform an aeroelastic analysis that considers horizontal and vertical lifting surfaces simultaneously, the governing equation in the TSD scheme should be modified. However, in this case, modification of the typical TSD equation is complicated, and the level of computational efficiency may be low because variables of several functions in the TSD equation are added. With the use of a multiblock approach, however, the TSD equation can be applied to combined models with horizontal and vertical lifting surfaces without requiring modifications of the TSD equation. As each domain, which is divided into horizontal and vertical lifting surface blocks, maintains the typical grid system of the TSD equation, the TSD equation is applied to each block without modifying the governing equation, and the efficiency of the TSD equation can be preserved. To perform aeroelastic analysis successfully using a multiblock approach, the applications of the appropriate interpolation methods are needed because the grid points on the block interface between the horizontal and vertical lifting surface blocks do not coincide with each other. That is, the grid lines in the vertical direction of the global coordinate are not placed continuously. The potential values should be shared between the horizontal and vertical lifting surface blocks to calculate the aerodynamic forces. To achieve this, an interpolation method is used. Although there are many interpolation methods, two approaches are suitable for this scenario. The first involves the use of a single global function, and the second uses a collection of local functions. In the former approach, the procedure often becomes too complicated to manage as the number of given data points increases. Moreover, the surface resulting when using the former approach occasionally exhibits excessive undulations [14]. In this study, the potential data are not regularly distributed on the block interface due to the sweptback wing configuration. Moreover, the gradient of potentials dramatically changes around the lifting surface in the transonic flow region. For these reasons, the latter approach is more suitable for this research. Akima proposed a bivariate interpolation method using local functions [14–17]. Furthermore, depending on the grid interface characteristics, different interpolation methods are applied at a computational cost. From regular grid points, such as a rectangular grid system to an irregular system, the rectangular-grid-data interpolation method is used [17]. In contrast, the interpolation method is applied for irregularly distributed data points [14].

In this study, the aeroelastic analysis method without a modified TSD equation for the combined model, including horizontal and vertical lifting surfaces, is introduced. As the global grid system of the horizontal and vertical tails is divided into respective typical TSD grid systems using a multiblock approach, the TSD equation is easily applied to the divided blocks. Inevitably, nonmatching grid points exist on the interface between the blocks. An imaginary plane with the potential block and grid points of the adjacent block should be fabricated to transfer the potentials efficiently. Thus, interpolation is required on the block interface. In this study, bivariate interpolation is applied, rather than interpolations such as the infinite plane spline method, because the local potentials change rapidly in transonic flow regions. In this case, the rectangular-grid-data interpolation and irregularly distributed data point interpolation methods are used for computational efficiency due to the characteristics between the interface of the block and the imaginary plane. Using these analysis systems with a multiblock approach, the aerodynamic results between the present equation and the Euler equations for the horizontal and vertical tail model are compared. Finally, the aeroelastic effects of the vertical tail are investigated in a comparison of the aeroelastic analysis results between the models with and without the vertical tail.

## II. Theoretical Background

### A. Unsteady Transonic Small Disturbance Equation

Although Navier–Stokes equations are the most accurate aerodynamic equation, many flow features depend on a precise evaluation of the viscous and turbulent terms. If the thickness value of a wing section is small and there is no boundary-layer separation, viscosity has little effect on the flowfields. If the viscous terms are removed from the Navier–Stokes equations, the equations become Euler equations. Furthermore, if the flow around the aircraft wing is irrotational and the perturbation is small, the TSD theory can be applied. A three-dimensional unsteady transonic small disturbance equation may be written in conservation law form as [18]

$$\frac{\partial f_0}{\partial t} + \frac{\partial f_1}{\partial x} + \frac{\partial f_2}{\partial y} + \frac{\partial f_3}{\partial z} = 0 \tag{1}$$

where

$$f_0 = -A\phi_t - B\phi_x \qquad f_1 = E\phi_x + F\phi_x^2 + G\phi_y^2$$
$$f_2 = \phi_y(1 + H\phi_x) \qquad f_3 = \phi_z$$

The preceding equations are given in a physical coordinate system $(x, y, z, t)$, and the subscripts $x$, $y$, and $z$ denote the derivative of the streamwise, spanwise, and vertical directions, respectively. The values of $t$ and $x$, $y$, and $z$ are nondimensionalized by $U/c_r$ and $c_r$, respectively. The disturbance velocity potential is represented by $\phi$. The coefficients $A$, $B$, and $E$ are defined as

$$A = M^2 \qquad B = 2M^2 \qquad E = 1 - M^2$$

where $M$ is the freestream Mach number, and the other coefficients $F$, $G$, and $H$ can be chosen depending upon the assumptions used when deriving the TSD equation. The coefficients are herein defined as

$$F = -\frac{1}{2}(\gamma + 1)M^2 \qquad G = \frac{1}{2}(\gamma - 3)M^2 \qquad H = -(\gamma - 1)M^2$$

where $\gamma$ is the specific heat ratio and $F$, $G$, and $H$ are NASA Ames coefficients. These coefficients depend on the assumptions made when deriving the TSD equation [11].

The TSD equation can be solved using a time-accurate AF method. The AF algorithm consists of a Newton linearization procedure coupled with an internal iteration technique [10]. The solution process involves two steps. First, a time linearization step is performed to estimate the potential field. Second, internal iterations are performed to minimize the linearization and factorization errors. The conditions imposed on the outer boundary of the computational domain are applied to nonreflecting boundary conditions [10]. To capture the shock efficiently in transonic and supersonic flowfields, the Engquist–Osher upwind scheme is implemented in the AF algorithm. To solve the governing equation numerically, the equations are transformed so that a swept-tapered wing can be analyzed using a finite difference grid. The finite difference grids in both the physical and computational domains are contained within rectangular boundaries and aligned with the leading and trailing edges of the lifting surfaces. Regions in the physical domain are mapped onto rectangular regions in the computational domain using

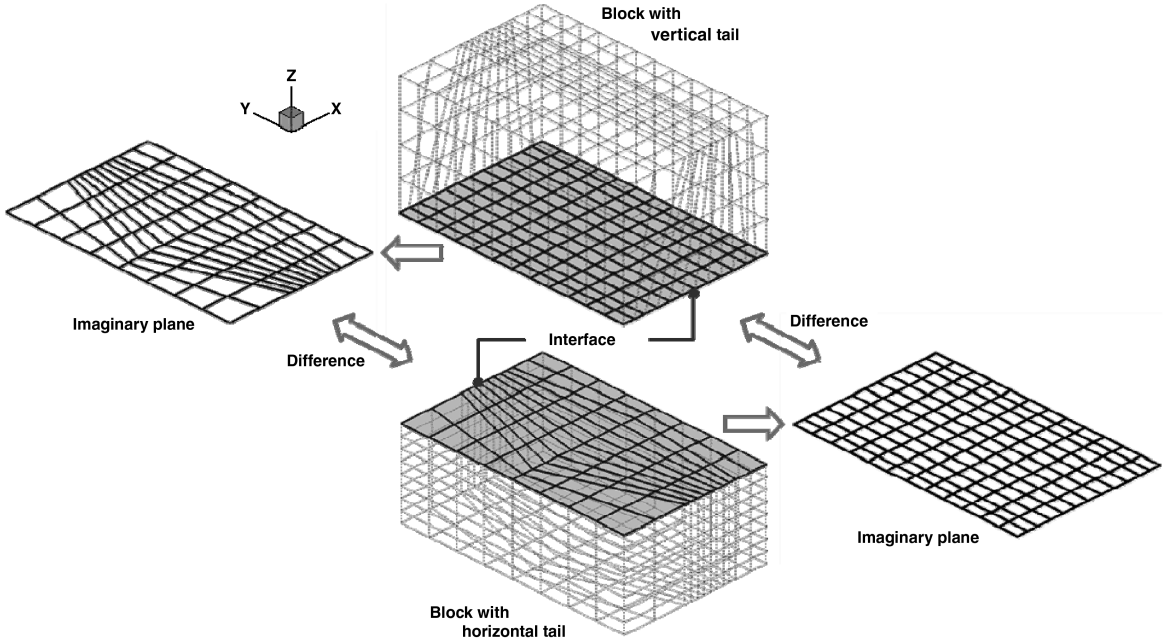


**Fig. 1 Schematic illustration of application of multiblock approach.**

a shearing transformation. The transformed equation is obtained using the modified shearing transformations [9].

### B. Aeroelastic Equation of Motion

The aeroelastic equation of motion for elastic models can be formulated in terms of the structural displacement vector $\{\mathbf{u}(t)\}$ using the Hamilton principle. It is written in matrix form as follows:

$$[M]\{\ddot{\mathbf{u}}(t)\} + [C]\{\dot{\mathbf{u}}(t)\} + [K]\{\mathbf{u}(t)\} = \{\mathbf{F}(t, \mathbf{u}, \dot{\mathbf{u}})\} \tag{2}$$

Here, $[M]$ is the mass matrix, $[C]$ is the damping matrix, $[K]$ is the stiffness matrix, and $\{\mathbf{F}\}$ is the external aerodynamic force vector

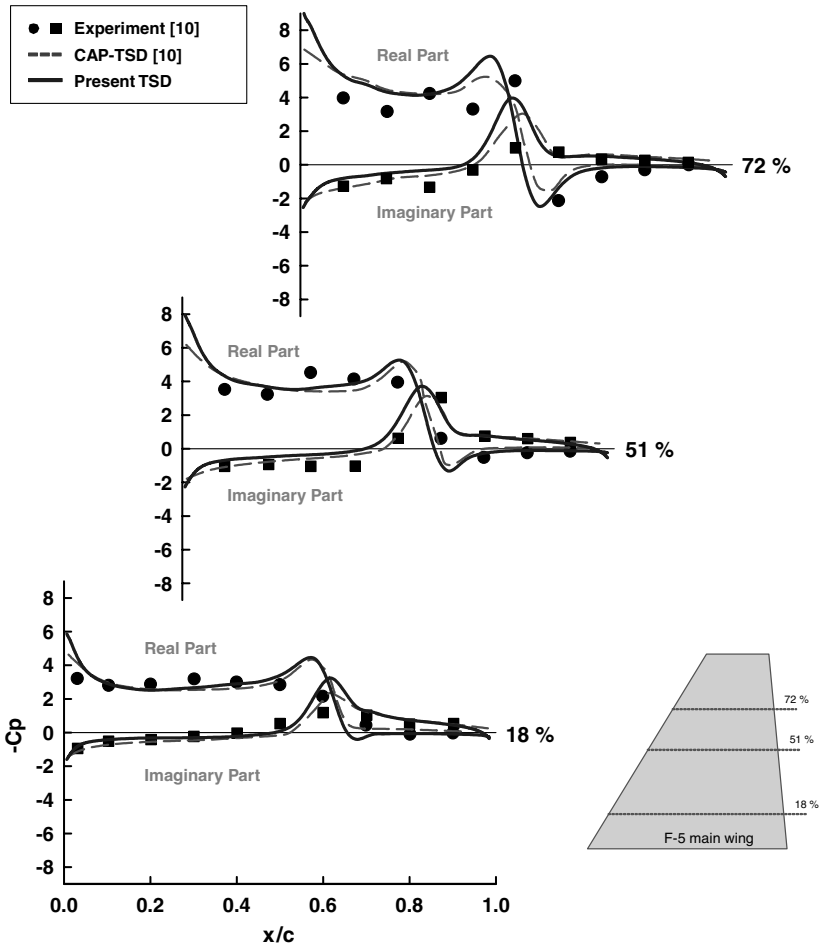


**Fig. 2 Comparisons of unsteady pressure coefficients on upper surface of F-5 main wing model at $M = 0.90$, $\alpha_0 = 0.0$ deg, $\alpha_m = 0.109$ deg, and $k = 0.137$ (CAP: Computational Aeroelasticity Program).**

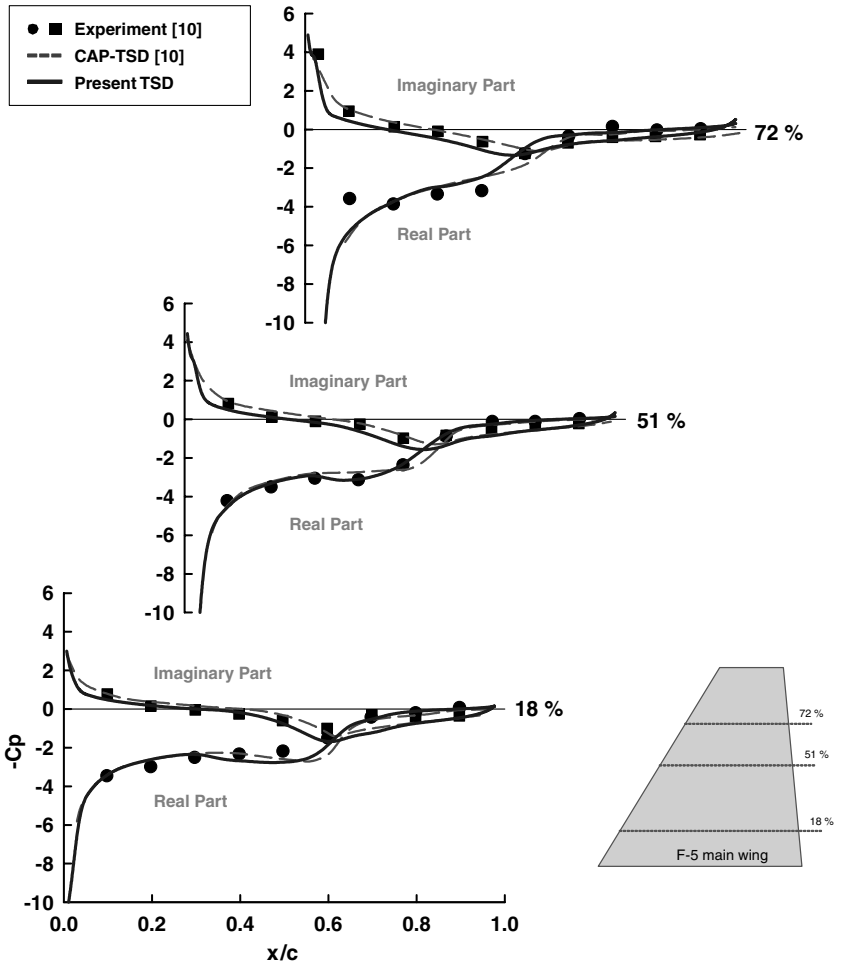


**Fig. 3 Comparisons of unsteady pressure coefficients on lower surface of F-5 main wing model at $M = 0.90$, $\alpha_0 = 0.0$ deg, $\alpha_m = 0.109$ deg, and $k = 0.137$.**

which is a time-dependent function of the displacement and velocity. The governing equation for linear elastic models is normally transformed to generalized coordinates for computational efficiency. It is assumed that the deformed shape of the elastic models can be represented by a discrete displacement vector $\{\mathbf{u}(t)\}$, which can be expressed as [19]

$$\{\mathbf{u}(t)\} = [\psi]\{\mathbf{q}(t)\} \tag{3}$$

where $[\psi]$ is the matrix of displacements of the natural vibration modes interpolated to the finite-difference grid points used to model the flow, and $\{\mathbf{q}\}$ is the generalized displacement vector.

Thus, the final matrix form of the aeroelastic equation of motion in the generalized coordinates can be recast as follows [4]:

$$[M_g]\{\ddot{\mathbf{q}}(t)\} + [C_g]\{\dot{\mathbf{q}}(t)\} + [K_g]\{\mathbf{q}(t)\} = \{\mathbf{Q}_g(t)\} \tag{4}$$

In the preceding equation, $[M_g]$, $[C_g]$, and $[K_g]$ are the generalized mass matrix, the generalized damping matrix, and the generalized stiffness matrix, respectively. The vector of the generalized forces $\{\mathbf{Q}_g(t)\}$ is defined by

$$\mathbf{Q}_g(t) = \frac{1}{2}\rho U^2 \int_s \Delta C_p h_i \, \mathrm{d}s \tag{5}$$

where $\rho$ is the freestream density, $U$ is the velocity of the freestream, $s$ is the area of the lifting surfaces, $\Delta C_p$ is the difference of the lifting pressure coefficients between upper and lower lifting surfaces, and $h_i$ is the $i$th vibration mode shape. The solution of Eq. (5) for each aerodynamic grid cell on the lifting surface is obtained using the $2 \times 2$ Gauss numerical integration method.

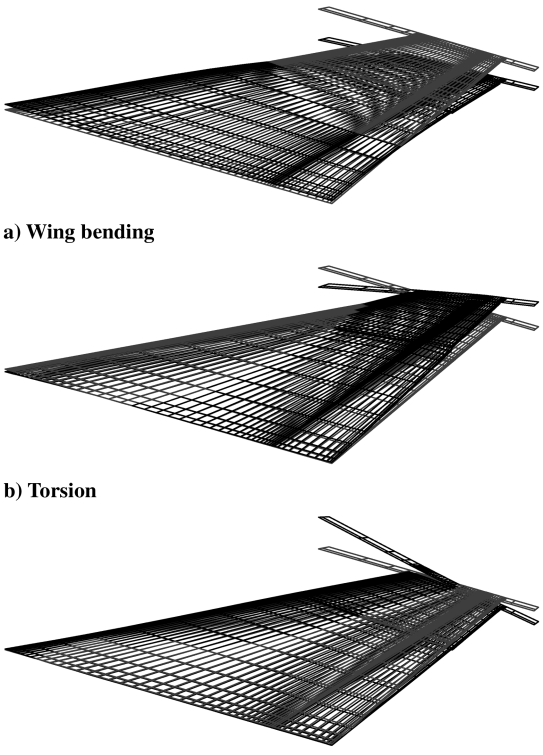

**a) Wing bending**

**b) Torsion**

**c) Forward wing torsion**

**Fig. 4 Splined mode shapes of F-16 main wing model.**

**Table 1 Comparisons of flutter velocity and frequency between experiment and analyses at $M = 0.90$**

| Vibration analysis | | Flutter analysis, DLM [21] | | Flight test [21] | | Present, TSD | |
|---|---|---|---|---|---|---|---|
| Mode | $F_n$, Hz | $V_f$, KCAS | $F_f$, Hz | $V_f$, KCAS | $F_f$, Hz | $V_f$, KCAS | $F_f$, Hz |
| Wing bending | 9.191 | 745.2 | 9.37 | 585 | 9.5 | 628.2 | 9.29 |
| Torsion | 9.964 | —— | —— | —— | —— | —— | —— |
| Forward wing torsion | 10.246 | 442.4 | 10.17 | —— | —— | —— | —— |

The aeroelastic solution procedure for integrating Eq. (4) has a state equation formulation. Equation (4) can be rewritten as a normal mode equation expressed in first-order state-space form as

$$\{\dot{\mathbf{x}}(t)\} = [A]\{\mathbf{x}(t)\} + [B]\{\mathbf{y}(t)\} \tag{6}$$

where

$$[A] = \begin{bmatrix} [0] & [I] \\ -[M_g]^{-1}[K_g] & -[M_g]^{-1}[C_g] \end{bmatrix} \qquad [B] = \begin{bmatrix} [0] & [0] \\ [0] & [M_g]^{-1} \end{bmatrix}$$

$$\{\mathbf{x}(t)\} = \begin{Bmatrix} \{\mathbf{q}(t)\} \\ \{\dot{\mathbf{q}}(t)\} \end{Bmatrix} \qquad \{\mathbf{y}(t)\} = \begin{Bmatrix} \{0\} \\ \{\mathbf{Q}_g(t)\} \end{Bmatrix}$$

The solutions of Eq. (6) can be obtained using the fifth-order Runge–Kutta method.

### C. Interpolation on Block Interface

In many aerodynamic analyses of multibody configurations, it is difficult to generate a reasonable single grid to cover the entire flow domain. This problem increases the attractiveness of the multiblock method. One advantage of the multiblock method is that it can resolve the topological complexity of a complicated geometry model by permitting grid components to be generated individually and thus be easily fitted with local boundary geometry. Another advantage is that the grid lines do not need to be continuous across grid interfaces. Local grid refinement and adaptive redistribution can be conducted more easily to accommodate different physical length scales. Finally, the method also provides a natural route for parallel computation [20].

To make good use of the multiblock approach, it needs to handle the grid interface appropriately within the flow solver. A schematic for the multiblock approach using the TSD equation is illustrated in Fig. 1. For the horizontal and vertical tail model, the global grid system is divided into two blocks, with each interface of each block having different grid points. Whereas the interface of the horizontal tail block has swept grid points as it is parallel to the horizontal tail, the interface of the vertical tail block has rectangular grid points because the interface is the perpendicular plane of the vertical tail. If the central difference is formulated on the grid points of the bottom of

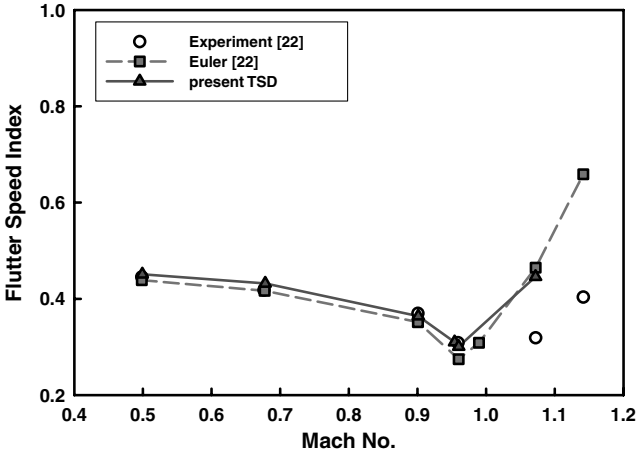


**a) Flutter speed boundary**

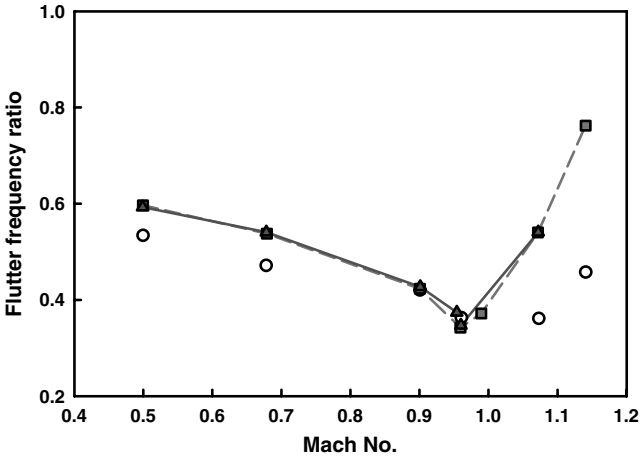


**b) Flutter frequency boundary**

**Fig. 5 Flutter boundaries of AGARD 445.6 wing model.**

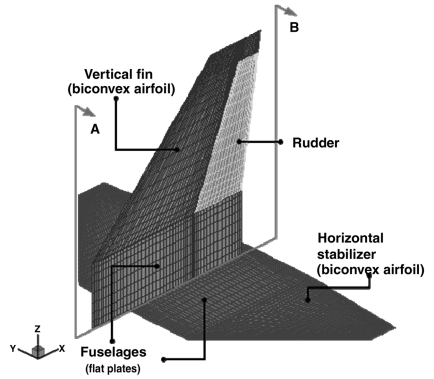


**Fig. 6 Aerodynamic surface grid of horizontal and vertical tails model.**

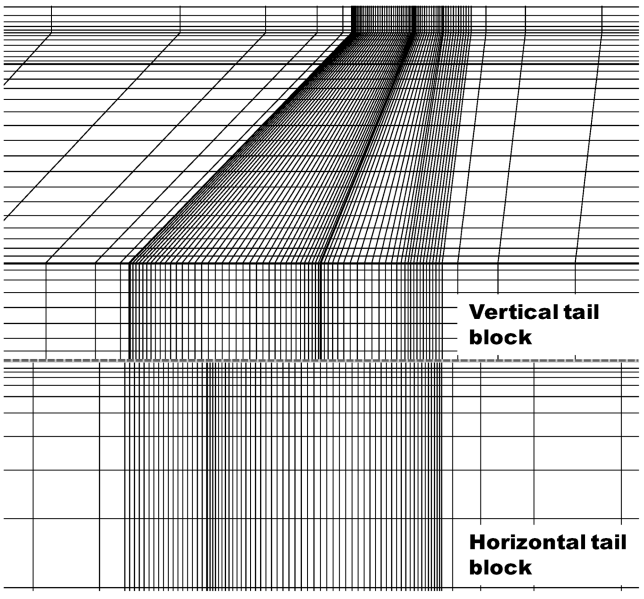


**Fig. 7 View of midplane ($A$–$B$ plane) of grid around the vertical fin.**

the vertical tail block, which is also the block interface, there is no problem for the grid points just above the bottom plane. However, there is no method for the grid points just below the bottom plane because the grid points between the bottom and the plane do not match. Thus, an imaginary grid plane of the bottom is required to formulate the difference of the grid points between the interface and adjacent block continuously; interpolation can fabricate an imaginary grid plane with the same grid points of the bottom and the potential values of the adjacent interface just below the bottom plane. The procedure on the top of the horizontal tail block is identical to this procedure.

Generally, when data is distributed on the line $f = f(x)$, there is only one independent variable. The potential values, however, are scattered in the function of $z = z(x, y)$. Such bivariate potential data are not regularly distributed on the block interface due to the sweptback wing configuration. Moreover, the potential gradient changes dramatically around the lifting surfaces in transonic flow regions. To consider this, the bivariate interpolations in Akima (1978, 1996) are used in this paper [14,17]. According to the grid interface configuration, two types of bivariate interpolations are used. For a vertical tail block, the grid interface on the block is a rectangular grid because the $x$-$z$ planes along the perpendicular direction of the vertical tail surface have identical grid points. Rectangular-grid-data surface fitting is applied in this case [17]. On the horizontal tail wing block, however, the grid points are irregularly distributed due to the sweptback angle of the horizontal tail. In the former interpolation method, applications are limited to cases in which the values of the function are given at rectangular grid points on a plane; i.e., if a two-dimensional Cartesian coordinate system with $x$ and $y$ axes is assumed, the values of $z = z(x, y)$ must be given as $z_{ij} = z(x_i, y_j)$ in the $x$-$y$ plane, where $i = 1, 2, \ldots, n_x$ and $j = 1, 2, \ldots, n_y$. Because of such restrictions, interpolation for irregularly distributed data points is applied on the interface of the horizontal tail block [14]. This method is a type of bivariate interpolation and generally has a smooth surface fitting when the values of the function are given at irregularly distributed points in a plane, i.e., a case in which the $z$ values are given as $z_i = z(x_i, y_j)$, where $i = 1, 2, \ldots, n$. In this method, the $x$-$y$ plane is divided into a number of triangular cells, and a bivariate fifth-degree polynomial in $x$ and $y$ is applied to each cell. Interpolation of potential values in a triangle is based on the following assumptions:

1) The value of the function at point $(x, y)$ in a triangle is interpolated by a bivariate fifth-degree polynomial in $x$ and $y$:

$$z(x, y) = \sum_{j=0}^{5} \sum_{k=0}^{5-j} q_{ij} x^j y^k \tag{7}$$

In this assumption, there are 21 coefficients to be determined.

2) The values of the function and its first-order and second-order partial derivatives (i.e., $z$, $z_x$, $z_y$, $z_{xx}$, $z_{xy}$, and $z_{yy}$) are given at each vertex of the triangle; this assumption yields 18 independent conditions.

3) The partial derivative of the function differentiated in the direction perpendicular to each side of the triangle is a polynomial degree, therein the direction of the side of the triangle; from this, three additional conditions are yielded.

Using the aforementioned procedure, a polynomial function can be found in each grid. The potential value in one block can be transferred to another block. The potential information is transferred between the horizontal and vertical blocks. More details of the interpolation method schemes are discussed in Akima (1978) [14]. For rectangular grid interpolation, the triangulation procedure can be removed. The triangulation algorithm requires a long computation time that is proportional to the cube of the number of grid points [14]. Thus, the rectangular grid interpolation uses less computational time compared with the irregular type. For higher computational efficiency, the interpolation methods are applied depending on the grid characteristics between the blocks.

## III. Numerical Results and Discussion

The aeroelastic analysis system using the TSD equation was verified in comparisons of the aerodynamic and aeroelastic results with the results for several different wings. The multiblock approach was applied to the verified aeroelastic analysis system to perform aeroelastic analysis of the combined model with the horizontal and vertical lifting surfaces. For the combined model, aerodynamic analysis is performed using the TSD equation with the multiblock approach and the results are compared with those of the Euler code. An aeroelastic analysis is also performed. Through comparisons of the aeroelastic results of the combined model and the horizontal-only model, the aeroelastic effects of the vertical tail are investigated.

### A. Verification of Aeroelastic Analysis System

To verify the aerodynamic analysis using the TSD equation, an unsteady aerodynamic analysis was performed for the F-5 main wing model oscillating with an amplitude of $\alpha_m = 0.109$ deg at $M = 0.90$, an initial angle of attack of $\alpha_0 = 0.0$ deg, and a reduced frequency of $k = 0.137$. The wing model has a full-span aspect ratio of 3.16, a taper ratio of 0.28, and a leading-edge sweep angle of 31.9 deg. Its section airfoil is NACA 65A004.8. Figure 2 shows the comparisons of the unsteady pressure coefficient on the upper surface at 18, 51,

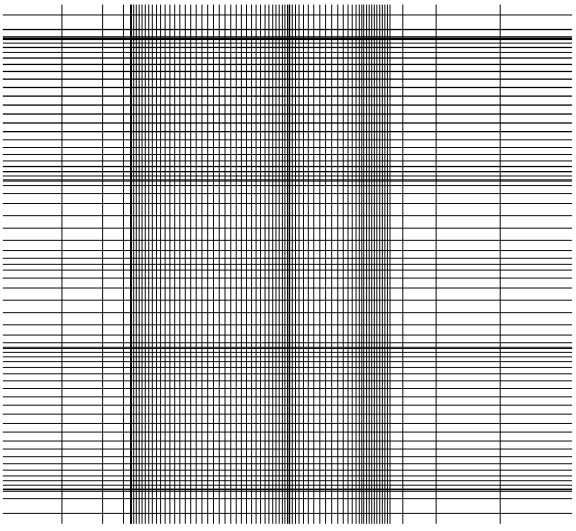

a) Grid points on the interface of the vertical tail block

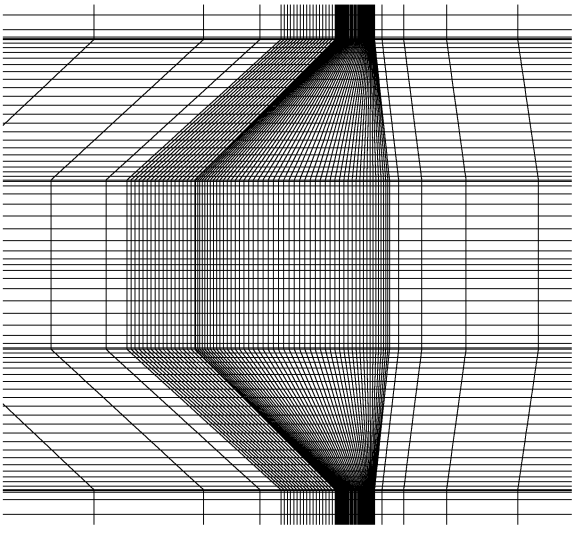

b) Grid points on the interface of the horizontal tail block

**Fig. 8 Comparisons of grid points on each interface.**

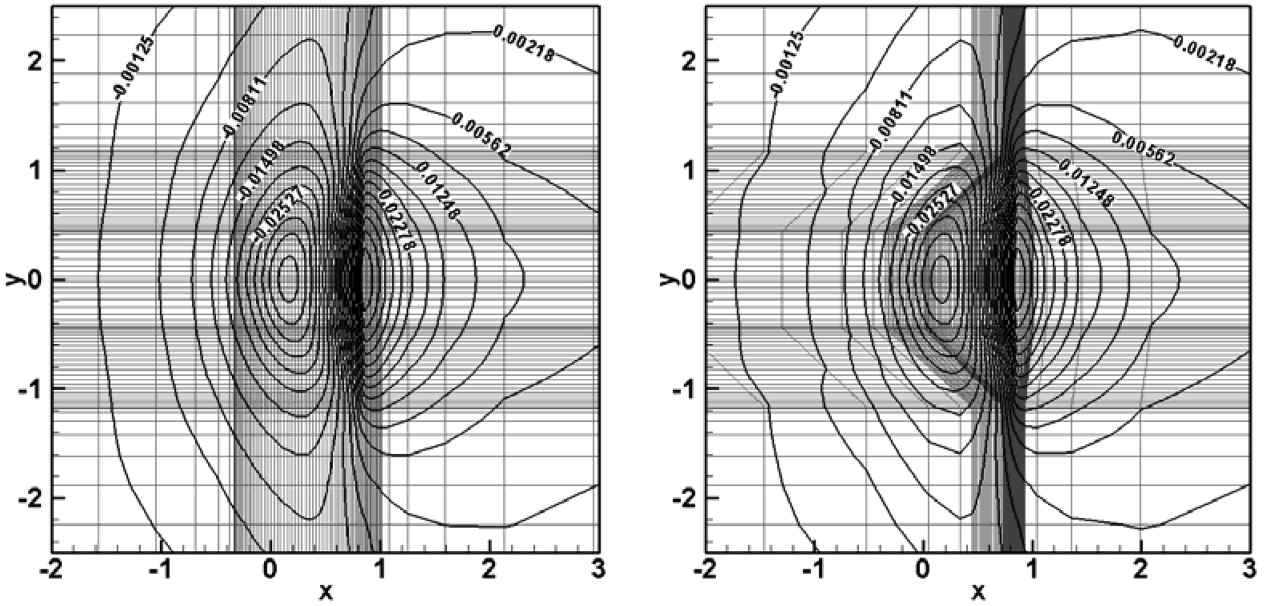


a) Interpolation on the interface from vertical block to horizontal block

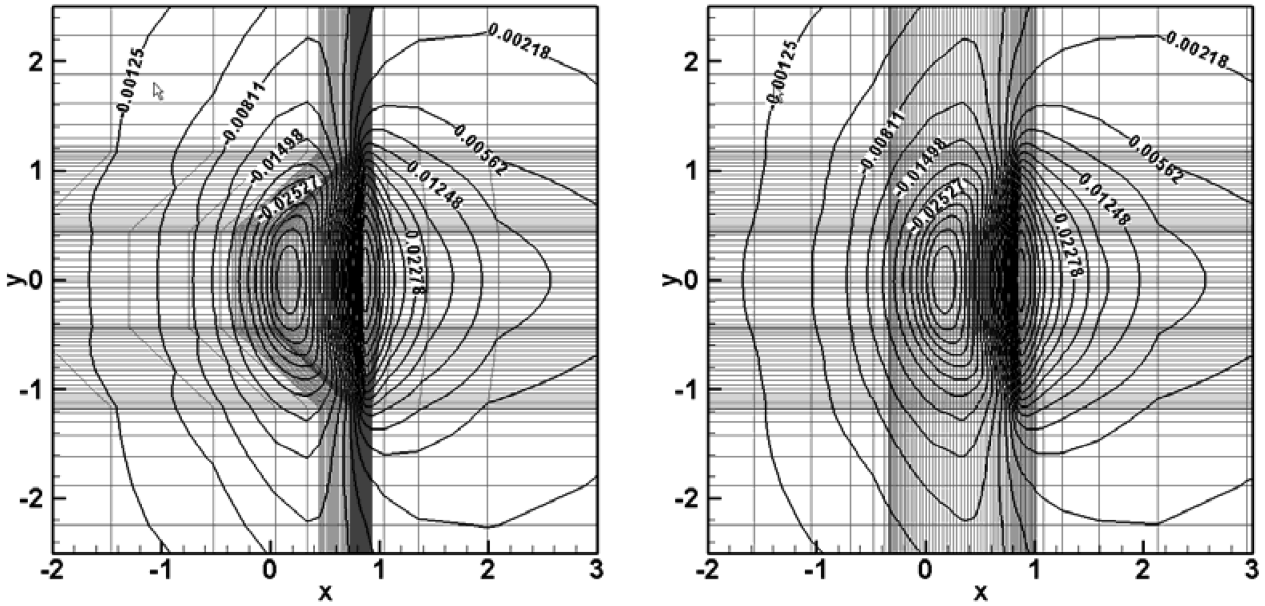


b) Interpolation on the interface from horizontal block to vertical block

**Fig. 9 Comparisons of velocity potentials on interfaces at $M = 0.90$.**

and 72% semispans with the experimental data and the analysis result of the TSD equation from [10]. It is shown that the present results agree well with the data, and these results are very similar to those from the TSD equation. Both the real and imaginary parts of the unsteady pressure coefficient show a jump at approximately half of a chord due to the shock wave. Comparisons of the unsteady pressure coefficient on the lower surface of the wing at the same three spanwise stations are shown in Fig. 3, and the present results are in a good agreement with experimental data.

Aeroelastic analyses were performed on several wing models to verify the aeroelastic analysis using the TSD equation. First, the present aeroelastic analysis system using the TSD equation was verified using the flight test data of an F-16 main wing model. The wing has a full-span aspect ratio of 3.2 and a leading-edge sweep angle of 40.0 deg. Its section airfoil is NACA 65A204. The configuration of the wing is referred to in the aerodynamic grid in [21]. The structural grid points, modal deflections, and frequencies were obtained from the appendix of the referenced study. The first three modes, wing bending, torsion, and forward wing torsion, used in this aeroelastic analysis are identical to those in [21]. To derive the mode spline in the aerodynamic coordinates, the wing should be divided into three parts: the wing, the control surface, and the launcher. After obtaining the mode spline, the divided parts are reunited in the aerodynamic coordinate.

Figure 4 shows the splined mode shapes compared with the aerodynamic grid. The analysis and experimental results for the flutter velocity and frequency at $M = 0.90$ are summarized in Table 1. The flutter speeds are expressed in knots calibrated airspeed (KCAS). The table includes the results from [21] using the double lattice method (DLM) code that is based on a linear aerodynamic equation. The DLM code predicts that flutter occurs at a speed of 745.2 KCAS with an approximate second natural frequency of 9.37 Hz, although the hump of the forward wing torsion mode is an exception due to the consideration of the structural damping of the wing. The present aeroelastic results using the TSD equation also predict the same flutter mode of wing bending with an approximate second natural frequency of 9.29 Hz, however, the flutter speed, 628.2 KCAS, is much closer to the flight test compared with the DLM analysis results [21].

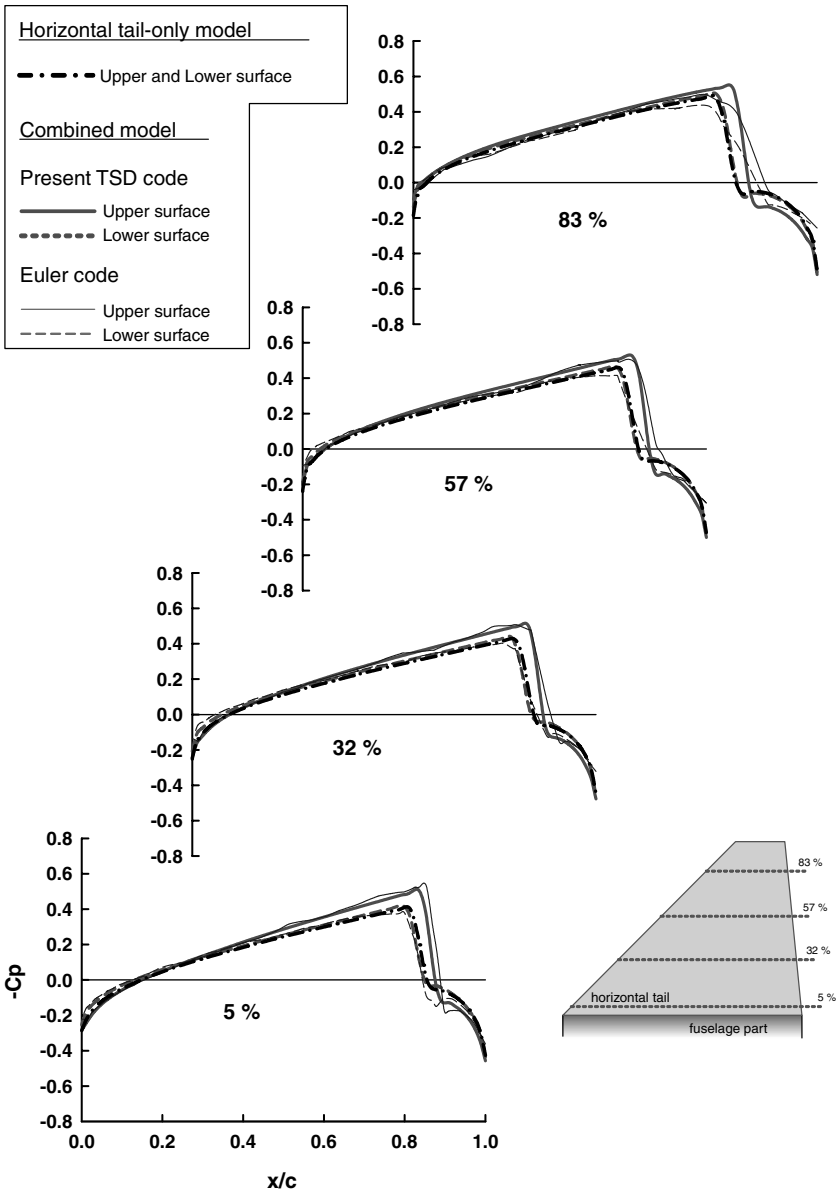


**Fig. 10 Comparisons of steady pressure coefficient on horizontal tail at $M = 0.90$ and $\alpha_0 = 0$ deg.**

Second, aeroelastic analysis of the AGARD 445.6 wing model was performed. The analysis results were compared with the experimental data and results of the Euler equations from [22]. The wing model has a panel aspect ratio of 1.65, a taper ratio of 0.66, and a quarter-chord sweep angle of 45 deg with a NACA 65A004 airfoil section. The first four elastic modes, representing the first bending, first torsion, second bending, and second torsion, are used in this aeroelastic analysis. The modes have sequential natural frequencies of 9.6, 38.17, 48.35, and 91.54 Hz, respectively, starting with the first mode [23]. The flutter boundary is computed for the subsonic and transonic flow regions, which are freestream Mach numbers ranging from 0.49 to 1.14. The present results using the TSD equation show good agreement with the experimental data and the results from the Euler equations in terms of the flutter speed and frequency for freestream Mach numbers below 1.0, as shown in Fig. 5. For freestream Mach numbers over 1.0, although they predict a premature rise compared with the experimental data, the computed results closely approximate the results of the Euler equations.

Through comparisons between the present results and the experimental data, as well as other analysis results of several wing models, it was verified that the present analysis system using the TSD equation provides accurate and reasonable aerodynamic and aeroelastic analysis results.

### B. Aeroelastic Analysis of Horizontal and Vertical Tails Model

Aeroelastic analysis of the combined model with the horizontal and vertical tails is accomplished using the TSD equation. The model involves three parts: horizontal stabilizers, a vertical fin, and the fuselage. Two horizontal tails are movable with hinge points at half-root chords, and the tail has an aspect ratio of 2.42, a taper ratio of 0.20, and a leading-edge sweep angle of 45.0 deg. The vertical tail uses a rudder as its control surface. The tail has an aspect ratio of 2.63, a taper ratio of 0.30, and a leading edge sweep angle of 43.0 deg. The root chord length of the vertical tail is 1.20 times that of the horizontal tail. As the distance between the leading edges of the root chords of the horizontal and vertical tails is 0.33, the leading edge of the vertical tail is in front of that of the horizontal tail. The aerodynamic grid system is shown in Fig. 6. In the aerodynamic analysis, the biconvex airfoil sections of the horizontal and vertical tails are used. The airfoil thickness of the horizontal tail changes linearly from 5.65% root chord to 4.0% tip chord. For the vertical tail, the airfoil thickness of the root chord is 5.0%, whereas that of the tip chord is 4.0%. The parts of the horizontal and vertical fuselages are regarded as flat plates. The $A$–$B$ plane, which is identical to the $x$-$z$ plane, is at the middle of the horizontal fuselage.

Figure 7 shows the grid points in the $A$–$B$ plane of Fig. 6, which includes the grid points of the vertical tail and the fuselage surfaces.

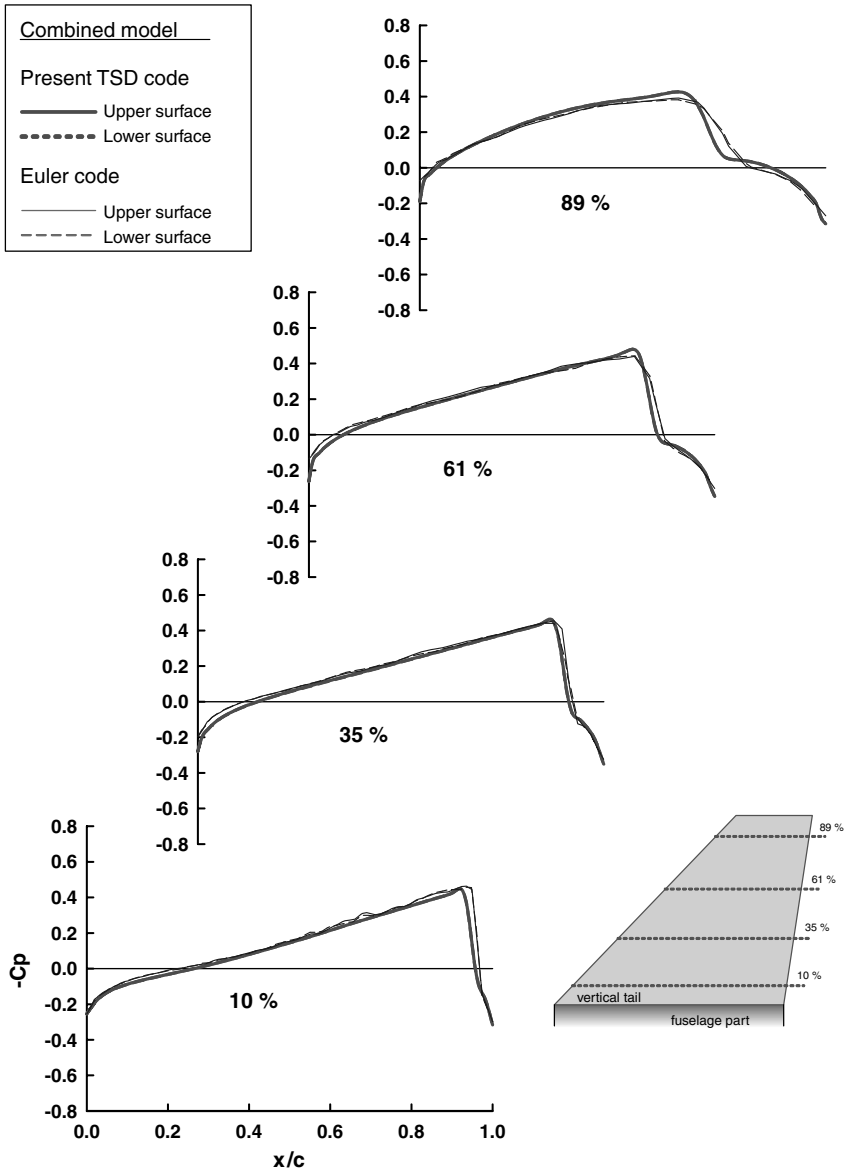


**Fig. 11 Comparisons of steady pressure coefficient on vertical tail at $M = 0.90$ and $\alpha_0 = 0$ deg.**

The interface, which has nonmatching grid points, is perceived between the horizontal tail and the vertical tail blocks because the normal directions of each lifting surface differ from each other. For more detailed nonmatching grid points, the grid points of the *x*-*y* plane on each interface are compared in Fig. 8.

The interface of the vertical tail block has a rectangular grid system, as shown in Fig. 8a, because the TSD grid points of the block are identical in the normal direction of the global *x*-*z* coordinate. The interface of the horizontal tail block, however, has a swept grid system, as shown in Fig. 8b, as the TSD grid points of the block are identical in the normal direction of the global *x*-*y* coordinate. There are clustered grid points in front of the leading edges of the horizontal tail and on the back of the trailing edges of the vertical tail for computational stability; the smooth interpolation on the grid points have sudden changes in their velocity potentials due to the differences in the positions of the leading edges and the length of the root chords between the horizontal and vertical tails. Figures 9a and 9b show comparisons of the instantaneous velocity potentials on the interface and the interpolated velocity potentials on the imaginary plane in the aerodynamic analysis at $M = 0.90$. The figures on the left side of Fig. 9 represent the velocity potential contours of the interfaces of each block. Those on the right are the interpolated velocity potential contours from the interfaces to the imaginary planes. In this transonic flow region, intense changes of the velocity potential values are observed due to the shock waves within the tail surfaces. The interpolated velocity potentials in each imaginary plane are almost equal to those of each interface. As the interpolation results between the interfaces are accurate even for severe cases with a rapid gradient of the velocity potentials, it is clear that the multiblock approach can be successfully applied to the TSD equation.

Steady aerodynamic analyses were performed for the combined model with horizontal and vertical tails using the TSD equation with the multiblock approach. The results of the TSD equation were then compared with those of the Euler equations, and FLUENT was used to obtain the aerodynamic analysis results of the Euler equations. Figure 10 shows the comparisons of the steady pressure coefficient on the upper and lower surfaces at 5, 32, 57, and 83% semispans of the horizontal tail with the Euler results. The solid lines are the steady pressure coefficients on the upper surface, and the dashed lines are those on the lower surface. The thin lines are the aerodynamic analysis results of the Euler equations, and the thick lines represent those of the TSD equation. The dash-dot lines are the steady pressure coefficients on the upper and lower horizontal surface for the horizontal tail-only model. In this case, the freestream Mach number $M$ is 0.9 and each angle of attack $\alpha_0$ of the horizontal and vertical tails is 0.0 deg. Weak shock waves were observed on both the upper and lower surfaces. For the horizontal tail-only model, the coefficients on

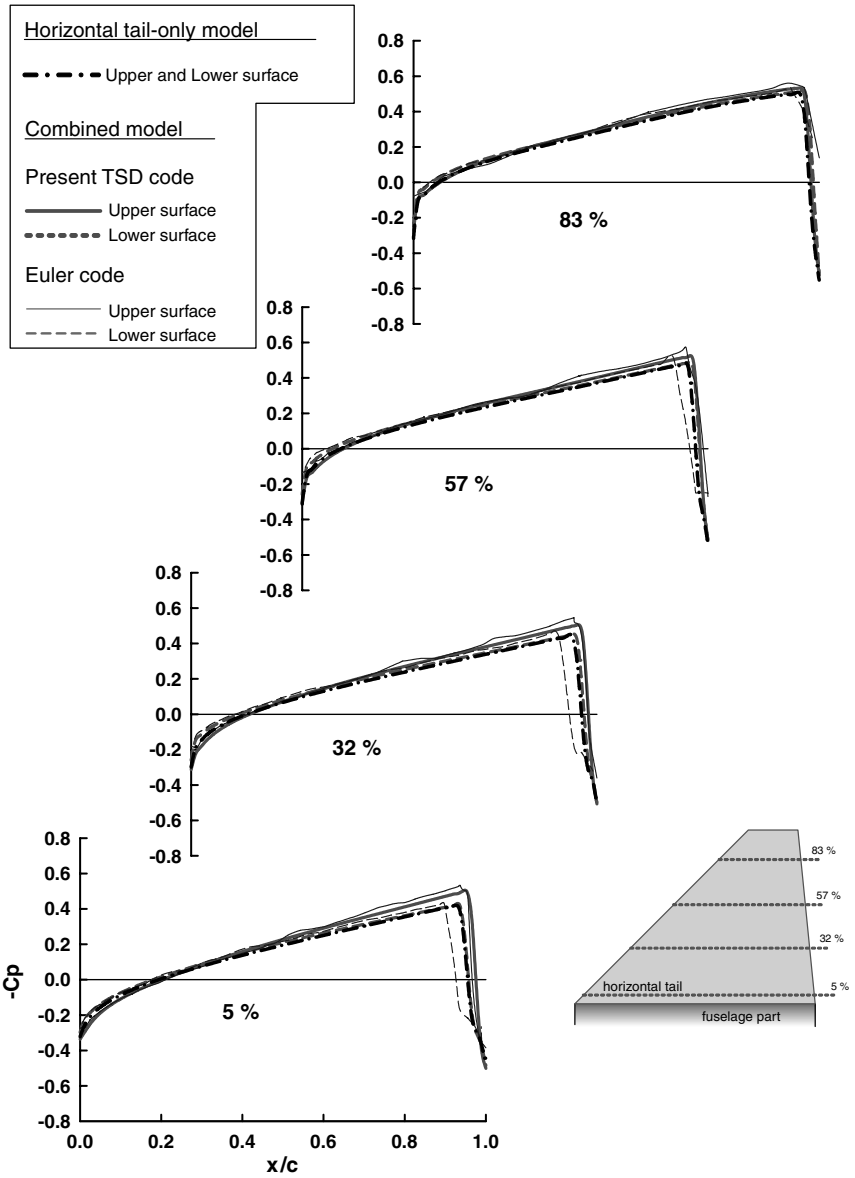


**Fig. 12 Comparisons of steady pressure coefficient on horizontal tail at $M = 0.95$ and $\alpha_0 = 0$ deg.**

the upper horizontal surfaces are identical to those on the lower surface because of the biconvex airfoil section of the horizontal tail and the 0.0 deg angle of attack. There is, however, a discrepancy between the upper and lower surfaces due to the aerodynamic interference between the upper surface of the horizontal tail and the vertical tail. These aerodynamic characteristics are identical to the results of the Euler equations. Figure 11 shows comparisons of the steady pressure coefficient at 10, 35, 61, and 89% semispans of the vertical tail with the Euler results. The solid lines are the steady pressure coefficients on right side surface and the dashed lines are those on left side surface; the meaning of each line thickness is the same as in Fig. 10. Weak shock waves exist within the surface of the vertical tail as in the case of the horizontal tail. The steady pressure coefficients between the right side and left side surfaces are identical due to the symmetric interference with the horizontal tail from the biconvex airfoil section and the 0.0 deg angle of attack of the vertical tail. The present results using the TSD equation show good agreement with those achieved using the Euler equations at each spanwise station. Figures 12 and 13 show the comparisons of the steady pressure coefficient with the Euler equations for the horizontal tail and the vertical tail at $M = 0.95$, respectively. For the pressure coefficients, the aerodynamic features on the horizontal tail and the vertical tail surfaces are identical to those in the previous case. In this case, the shock wave is located near the tip and trailing edges, but not within the surfaces. Although the predicted positions of the shock waves between the TSD and Euler equations are minutely different, the comparisons show good agreement. For the case of Figs. 10 and 11, it seems that the sharpness of the shock wave obtained from the Euler code becomes smaller compared with those near the fuselage due to the effect of the rotational flows in tail tip. However, there is the discrepancy between the present TSD results and the Euler results near the tail tip because the present TSD code has the assumption of irrotational flows. For the case with very strong shock waves shown in Figs. 12 and 13, the shock wave computed using the TSD equation is backward compared with the shock position predicted by the Euler equations. This feature is obvious as the gradient of the pressure coefficients changes rapidly. The dense shock waves are located near the tail tip due to the forward trailing-edge angle of the horizontal tail model. On the other hand, those appear near the fuselage due to the backward trailing-edge angle of the vertical tail model. Therefore, there are the discrepancies at the 32 and 57% span positions in Fig. 12 and the 89% span position in Fig. 13. The positions of dense shock waves can be confirmed from the steady pressure contours in Fig. 14. Figure 14a shows the steady pressure contours on the upper surface of the horizontal tails and the left side surface of the vertical tail at $M = 0.90$. It is shown that the shock waves on each tail surface are connected through the horizontal and vertical fuselage surfaces. Figure 14b shows the steady pressure contour at $M = 0.95$. In this

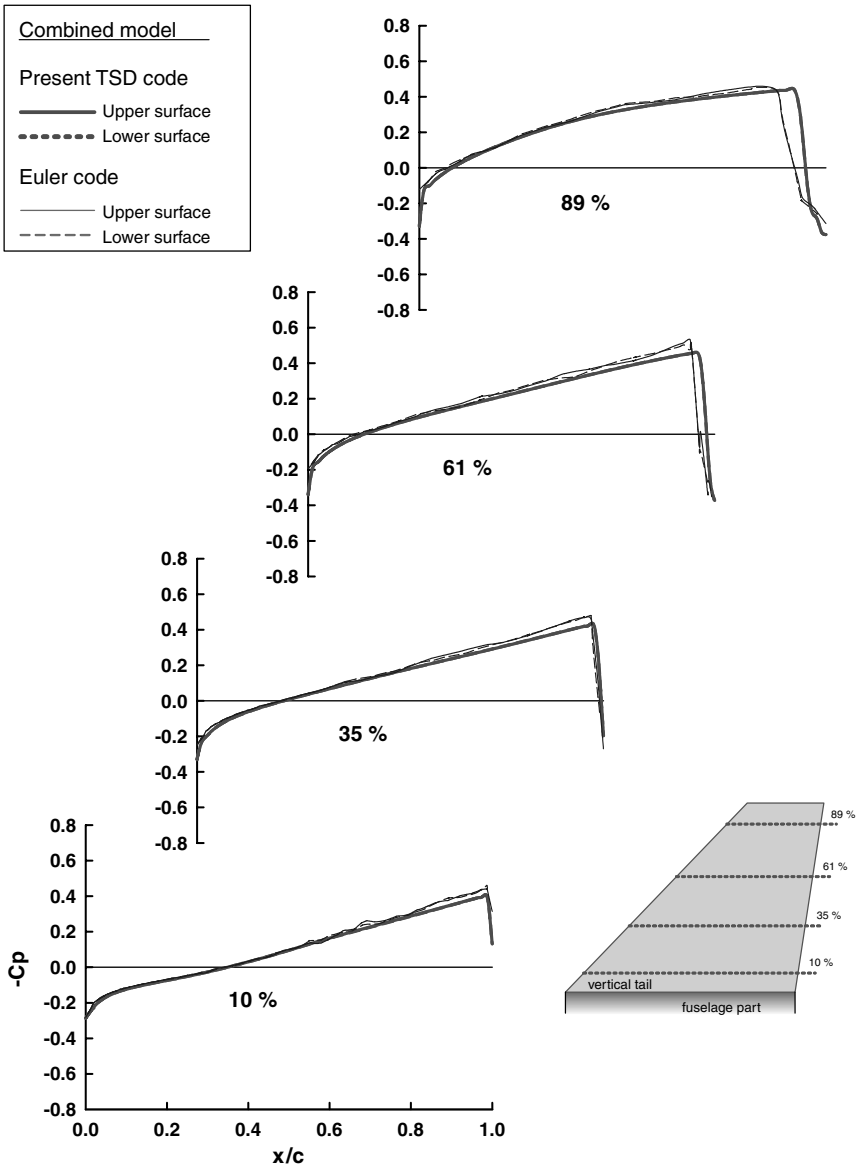


**Fig. 13 Comparisons of steady pressure coefficient on vertical tail at $M = 0.95$ and $\alpha_0 = 0$ deg.**

case, only the shock waves of the horizontal tail are connected through the horizontal fuselage surface, and the shock wave of the vertical tail is present only on the tip edges.

The natural mode shapes and frequencies are obtained from the structural analysis using an MSC/NASTRAN. The boundary condition of the structural model is modeled as only being clamped at the bottom node point of the leading-edge line of the vertical fuselage. Generally, aeroelastic analysis requires a data transfer stage between the structural node and aerodynamic grid points because they are subject to different engineering considerations. In this study, the mode shapes of the structural node points are interpolated to the aerodynamic grid points using the infinite plate spline method.

Figure 15 shows comparisons between the structural node and aerodynamic grid points before the interpolation of the mode shapes is performed. When the spline method is applied to the interpolation, the two different length scales of the physical systems are considered carefully. If discontinuity exists in a rudder or in all movable tails, for example, the horizontal and vertical tail structures are divided into several parts, such as the control surfaces and the remaining parts. After individual interpolation of each part, the divided parts must be transferred independently and then superposed in the aerodynamic coordinate system. The first 29 elastic modes are used in the aeroelastic analysis of the combined model. The frequency of the first mode is 10.58 Hz and that of the last mode is 99.48 Hz. Several antisymmetric and symmetric mode shapes are shown in Figs. 16 and 17, respectively. The mode shapes are the splined results to the aerodynamic grid points. The antisymmetric and symmetric mode shapes are sorted based on the shapes of the right and left horizontal tails. The first mode represents bending mode shapes on each tail in a clockwise direction, and the second mode has coupled shapes with the entire bending mode of the horizontal fuselage and antisymmetric rotating modes of the horizontal tails.

Aeroelastic analyses of the combined model with horizontal and vertical tails were performed in the transonic region, and the aeroelastic characteristics between the combined mode and the horizontal tail-only model were investigated by comparing the aeroelastic time responses. In the aeroelastic equation of motion for the horizontal tail-only model, the mass, damping, and stiffness matrices are identical to those of the combined model, but the aerodynamic forces of the vertical tail are not coupled with the structural vertical tail. Figure 18 shows the first modal time responses of the two models at Mach 0.90 and 0.95. All cases have initial angles of attack of 0.0 deg on the horizontal and vertical tails. Comparisons of the time responses between the combined model and the horizontal tail-only model are shown in Fig. 18a. In this case, the freestream Mach number is 0.90 and the speed is 1294.0 KEAS (knots equivalent air speed). The thick line represents the time

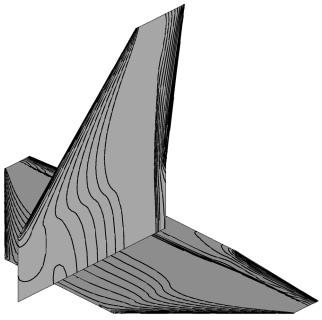

a) $M = 0.90$

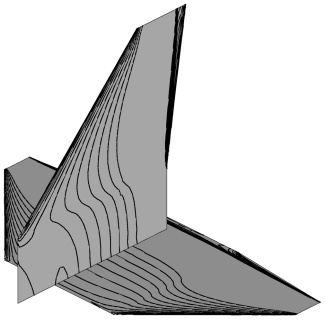

b) $M = 0.95$

**Fig. 14 Steady pressure contours at each Mach number and $\alpha_0 = 0$ deg.**

response of the combined model, and the thin line is that of the horizontal tail-only model. In the combined model, which considers the aerodynamic effects of the vertical tail, flutter occurs as shown by the neutral response, but the horizontal tail-only model shows divergent time responses at the same speed. Figure 18b shows the comparisons of the time responses of the two models at $M = 0.95$ and 1365.9 KEAS. In contrast with the results of $M = 0.90$, the horizontal tail-only model has a neutral time response, but it is apparent that flutter had already appeared at the same speed for the combined model. The source of discrepancy in the aeroelastic characteristics between the two Mach numbers may be the difference of the shock wave locations. For $M = 0.90$, the aerodynamic effects of the vertical tail may delay the flutter speed for the combined model, due to the shock waves connecting across the tails and fuselages as shown in Fig. 14. However, because the shock wave is only located on the tip edges of the vertical tail at $M = 0.95$, the local tip motion of the vertical tail of the combined model may put the flutter speed more forward compared with the horizontal tail-only model.

As shown in the results of Fig. 18, it is confirmed that the aeroelastic characteristics are different between the combined model with horizontal and vertical tails and the horizontal tail-only model. In particular, the accurate aeroelastic examinations are required for the case of the all-moveable horizontal tail because the structural stability of the tail is lower compared with other structures in an aircraft. For more accurate aeroelastic analysis of the horizontal tail, the aerodynamic effects of the vertical tail have to be concurrently considered with those of the horizontal tail. Although the Navier–Stokes or Euler equations can be used for the combined model directly, the equations incur a high computational cost. Also, it is difficult to treat the aerodynamic grid motions for control surfaces. Therefore, the present multiblock TSD approach may be one of the most efficient aeroelastic analysis methods for the combined model. It is easy to implement because the spline at the interface is only required without any labor.

## IV. Conclusions

Aerodynamic and aeroelastic analyses of the combined model with horizontal and vertical tails were performed using the TSD equation. The combined model is divided into a horizontal tail block and a vertical tail block, as the TSD equation is only applied for the

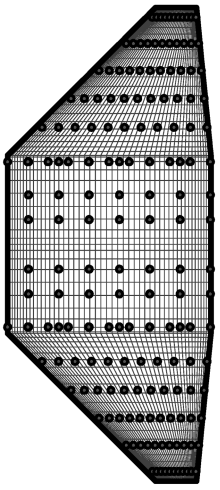

a) Horizontal tail

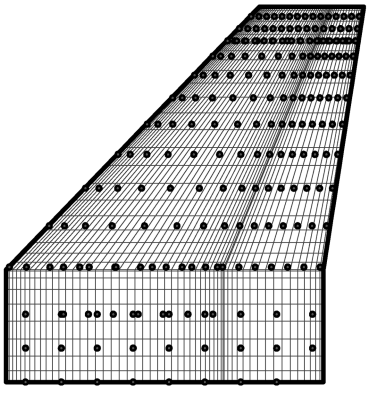

b) Vertical tail

**Fig. 15 Comparisons between structural nodes and aerodynamic grid points.**

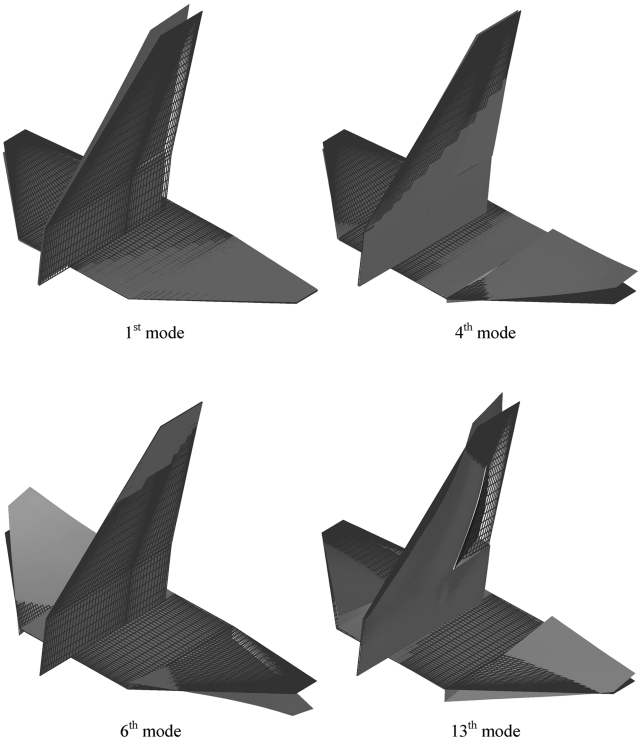


**Fig. 16 Antisymmetric elastic mode shapes of horizontal tail.**

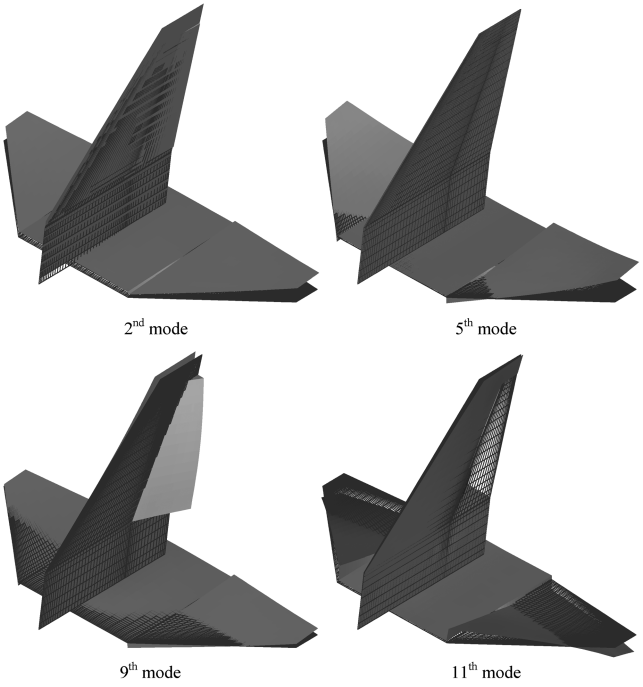


**Fig. 17 Symmetric elastic mode shapes of horizontal tail.**

models with lifting surfaces on identical or parallel planes. The divided blocks are then applied to the TSD equation individually. Nonmatching grid points exist on each interface between the blocks because the normal directions of the horizontal and vertical tail surfaces are different. For continuous formulations of the TSD equation on the interfaces, each block requires imaginary planes with potentials of the interface of the adjacent block and grid points on the interface of the block. Although several interpolation methods can be applied to fabricate the imaginary planes, the bivariate interpolation method is used in place of the other methods to take into account the rapid change of the local gradient of the velocity potentials.

The aeroelastic analysis system using the TSD equation was verified using comparisons with experimental data and other aerodynamic equation results from the literature regarding several different wing models. In the unsteady aerodynamic analysis of the F-5 main wing model, the present TSD results agreed well with the experimental data as well as other analysis results. For the AGARD 445.6 wing and F-16 main wing models, the aeroelastic analyses results showed good agreement with the results of the Euler equations and the experimental data. The multiblock approach was applied to the verified aeroelastic analysis system to perform an aeroelastic analysis of the combined model with horizontal and vertical tails. The aerodynamic analysis of the combined model was performed and the results were compared with those of the Euler code. The results show that the TSD equation can be applied in an aerodynamic analysis of a combined model with horizontal and vertical lifting surfaces without any modifications. Finally, the aeroelastic characteristics of the horizontal tail were investigated through comparisons of the aeroelastic time responses with and without the aerodynamic effects of the vertical tail in the transonic region. For the present model, the aerodynamic effects of the vertical tail aggravate the aeroelastic instability at $M = 0.95$ and worsen the instability at $M = 0.90$. It is expected that the contrasting results are related to the locations of the shock wave.

From the present aeroelastic results, the aeroelastic characteristics of the combined model with horizontal and vertical tails are different from those of the horizontal tail-only model. Also, the all-moveable horizontal tail is fragile relative to other fixed parts of an aircraft from the viewpoint of structural stability. Hence, aeroelastic analyses coupled between horizontal and vertical tails are required for more

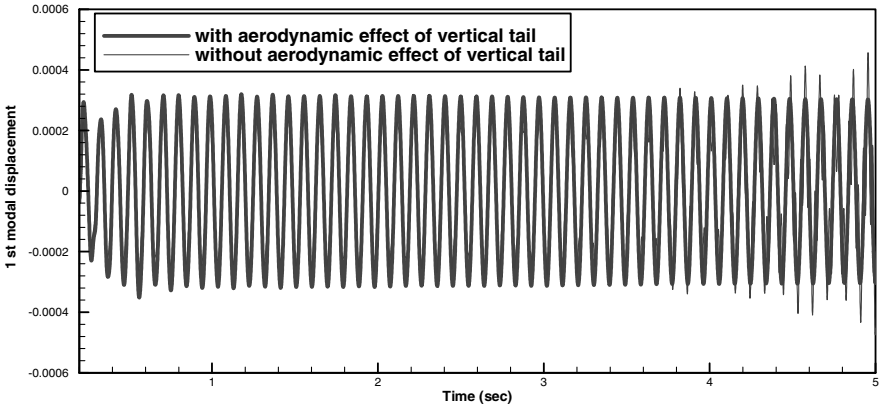


**a) $M$ = 0.90, $V$ = 1294.0 KEAS**

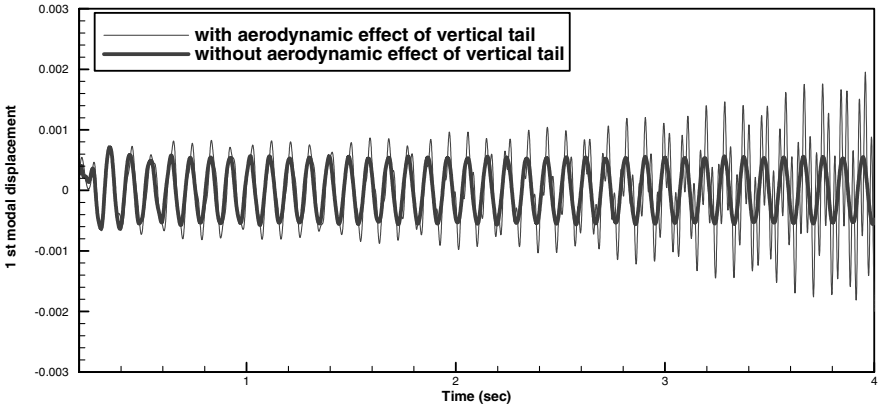


**b) $M$ = 0.95, $V$ = 1365.9 KEAS**

**Fig. 18 Comparisons of first modal displacements at each Mach number.**

accurate stability prediction. This approach will be expected as one of the practical aeroelastic analysis techniques considering conventional tail configurations.

## Acknowledgments

This work was supported by the second stage of the Brain Korea 21 Project in 2007, Korea Aerospace Industries, Ltd., and the Defense Acquisition Program Administration and Agency for Defense Development under contract UD070041AD.

## References

[1] Dowell, E. H., Crawley, E. F., Curtiss, H. C., Jr., Peters, D. A., Scanlan, R. H., and Sisto, F., *Modern Course in Aeroelasticity*, Kluwer Academic, Norwell, MA, 1995.

[2] Kim, D. H., Park, Y. M., Lee, I., and Kwon, O. J., "Nonlinear Aeroelastic Computation of a Wing/ Pylon/Finned-Store Using Parallel Unstructured Euler Solver," *AIAA Journal*, Vol. 43, No. 1, 2005, pp. 53–62. doi:10.2514/1.11011

[3] Kim, D. H., and Lee, I., "CFD-Based Matched-Point Transonic and Supersonic Flutter Computations Using a Modified TSD Equation," *Computational Fluid Dynamics Journal*, Vol. 11, No. 1, 2002, pp. 35–49.

[4] Kwon, H. J., Kim, D. H., and Lee, I., "Frequency and Time Domain Flutter Computations of a Wing with Oscillating Control Surface Including Shock Interference Effects," *Aerospace Science and Technology*, Vol. 8, No. 6, 2004, pp. 519–532. doi:10.1016/j.ast.2004.04.001

[5] Murman, E. M., and Cole, J. D., "Calculation of Plane Steady Transonic Flows," *AIAA Journal*, Vol. 9, No. 1, 1971, pp. 114–121.

[6] Rizzetta, D. P., and Chin, W. C., "Effect of Frequency in Unsteady Transonic Flow," *AIAA Journal*, Vol. 17, No. 7, 1979, pp. 779–781.

[7] Houwink, R., and van der Vooren, J., "Improved Version of LTRAN2 for Unsteady Transonic Flow Computations," *AIAA Journal*, Vol. 18, No. 8, 1980, pp. 1008–1010.

[8] Isogai, K., "Numerical Study of Transonic Flutter of a Two-Dimensional Airfoil," National Aerospace Lab., NAL TR-617T, Tokyo, July 1980.

[9] Guruswamy, G. P., and Goorjian, P. M., "Efficient Algorithm for Unsteady Transonic Aerodynamics of Low-Aspect-Ratio Wings," *Journal of Aircraft*, Vol. 22, No. 3, 1985, pp. 193–199.

[10] Batina, J. T., "Efficient Algorithm for Solution of the Unsteady Transonic Small-Disturbance Equation," *Journal of Aircraft*, Vol. 25, No. 7, 1988, pp. 598–605.

[11] Batina, J. T., Seidel, D. A., Bland, S. R., and Bennett, R. M., "Unsteady Transonic Flow Calculations for Realistic Aircraft Configurations," *Journal of Aircraft*, Vol. 26, No. 1, 1989, pp. 21–28.

[12] Batina, J. T., "Unsteady Transonic Flow Calculations for Interfering Lifting Surface Configurations," *Journal of Aircraft*, Vol. 23, No. 5, 1986, pp. 422–430.

[13] Gibbons, M. D., "Extending a Transonic Small Disturbance Code to Treat Swept Vertical Surfaces," AIAA Paper 92-2503-CP, 1992.

[14] Akima, H., "Algorithm 526: Bivariate Interpolation and Smooth Surface Fitting for Irregularly Distributed Data Points [E1]," *ACM Transactions on Mathematical Software*, Vol. 4, No. 2, 1978, pp. 160–164. doi:10.1145/355780.355787

[15] Akima, H., "New Method of Interpolation and Smooth Curve Fitting Based on Local Procedures," *Journal of the Association for Computing Machinery*, Vol. 17, No. 4, 1970, pp. 589–602. doi:10.1145/321607.321609

[16] Akima, H., "Method of Bivariate Interpolation and Smooth Surface Fitting Based on Local Procedures," *Communications of the ACM*, Vol. 17, No. 1, 1974, pp. 18–20. doi:10.1145/360767.360779

[17] Akima, H., "Algorithm 760: Rectangular-Grid-Data Surface Fitting That Has the Accuracy of Bicubic Polynomial," *ACM Transactions on Mathematical Software*, Vol. 22, No. 3, 1996, pp. 357–361. doi:10.1145/232826.232854

[18] Batina, J. T., "Unsteady Transonic Small-Disturbance Theory Including Entropy and Vorticity Effects," *Journal of Aircraft*, Vol. 26, No. 6, 1989, pp. 531–538.

[19] Yoo, J. H., Kim, D. H., Kwon, H. J., and Lee, I., "Nonlinear Aeroelastic Simulation of a Full-Span Aircraft with Oscillating Control Surfaces," *Journal of Aerospace Engineering*, Vol. 18, No. 3, 2005, pp. 156–167. doi:10.1061/(ASCE)0893-1321(2005)18:3(156)

[20] Liu, J., and Shyy, W., "Assessment of Grid Interface Treatments for Multi-Block Incompressible Viscous Flow Computation," *Computers and Fluids*, Vol. 25, No. 8, 1996, pp. 719–740. doi:10.1016/S0045-7930(96)00022-9

[21] Denegri, C. M., Jr., "Limit Cycle Oscillation Flight Test Results of a Fighter with External Stores," AIAA Paper 2000-1394, 2000.

[22] Lee-Rausch, E. M., and Batina, J. T., "Wing Flutter Boundary Prediction Using Unsteady Euler Method," AIAA Paper 93-1422, 1993.

[23] Yates, E. C., Jr., "AGARD Standard Aeroelastic Configuration for Dynamic Response, Candidate Configuration 1: Wing 445.6," NASA TM-100492, 1987.